

Phase Speed Cross Spectra of Eddy Heat Fluxes in the Pacific

RYAN ABERNATHEY *

Columbia University, New York, New York

CIMARRON WORTHAM

Applied Physics Laboratory, University of Washington, Seattle, Washington

**Corresponding author address:* Ryan Abernathey, Lamont-Doherty Earth Observatory, Palisades, NY.

E-mail: rpa@ldeo.columbia.edu

ABSTRACT

This study investigates the observed spectral character of eddy heat fluxes near the ocean surface, focusing on the distribution in wavenumber and phase-speed space. Eddy heat fluxes in the Eastern Pacific are calculated from concurrent satellite sea-surface height and sea-surface temperature data. At each latitude, wavenumber, frequency, and phase speed power spectra and cross spectra are constructed and presented as a function of latitude. These spectra reveal the dominance of coherent mesoscale eddies in both the length scale and phase speed of eddy heat fluxes. The breadth of the spectra are characterized via spectral moments; these moments show that the eddy fluxes are relatively concentrated around the dominant wavenumber and phase speed. The overall magnitude of the heat transport and eddy diffusivity are shown to compare well with previous studies. Implications for eddy parameterization are discussed.

1. Introduction

Transient motions (a.k.a. “eddies”) in the ocean and atmosphere lead to significant material transport. Of particular importance is the meridional eddy heat transport, which contributes to the maintenance of Earth’s pole-to-equator temperature gradient (Trenberth and Caron 2001; Wunsch 2005). Although eddy heat fluxes in the ocean are relatively less significant than in the atmosphere, they are still an important part of the ocean heat budget, particularly at regional scales and in the Southern Ocean (Jayne and Marotzke 2002; Volkov et al. 2008; Abernathey and Cessi 2014). Because of their relatively small spatial scales, ocean eddy fluxes are more difficult to observe than those in the atmosphere, and their statistical properties are less well characterized. Satellites provide a uniquely powerful tool for observing eddies at the ocean surface. Climate models are also beginning to resolve the ocean mesoscale (McClean et al. 2011).

A fundamental question is what determines the strength of the eddy flux and how this flux is related to more readily observable eddy properties such as eddy size, kinetic energy, etc. Inspired by the classical “mixing length” arguments of Taylor (1915) and Prandtl (1925) regarding turbulent fluxes, many studies have assumed the eddy flux in the ocean to be proportional to the background tracer gradient (i.e. that it is diffusive) and to the product of a characteristic eddy size and eddy velocity (e.g. Holloway 1986; Keffer and Holloway 1988; Held and Larichev 1996; Visbeck et al. 1997; Stammer 1998). More recent studies have added a new ingredient to the equation: the eddy phase speed, i.e. the eddy propagation relative to the background mean flow (Marshall et al. 2006; Smith and Marshall 2009; Abernathey et al. 2010; Ferrari and Nikurashin 2010; Klocker et al. 2012a,b; Abernathey and Marshall 2013). In particular, the simple stochastic model of Ferrari and Nikurashin (2010) demonstrates how zonal phase propagation suppresses meridional eddy diffusion and puts forth a quantitative theory for the magnitude of this effect.

The framework of Ferrari and Nikurashin (2010) was recently tested by Klocker and Abernathey (2014, henceforth KA14) in a comprehensive way using kinematic passive tracer

simulations in the east Pacific (the same sector studied here). Those results indicate that the extratropical meridional eddy flux of a passive tracer due to mesoscale eddy stirring could be parameterized quite well in terms of a single wavenumber and phase speed at each latitude. The appropriate phase speed is the long baroclinic Rossby wave phase speed, while the appropriate wavenumber is proportional to the average diameter of tracked nonlinear coherent eddies from the eddy census of Chelton et al. (2011). The fact that the eddy flux can be parameterized in terms of an essentially monochromatic model seems at odds with the fact that the ocean contains a broad spectrum of variability in space and time (Richman et al. 1977; Stammer 1997; Hughes and Williams 2010; Wortham and Wunsch 2014). Therefore, a key motivation for our study is to attempt to reconcile the success of the monochromatic FN10 model with the broadband nature of the variability. We wish to assess how narrowly concentrated the eddy flux is around a single length scale and phase speed.

To answer this question, we employ satellite observations to investigate the spectral character of surface eddy meridional heat fluxes over a wide range of latitudes. This is achieved by calculating wavenumber-frequency cross-spectra for sea-surface temperature (SST) and the geostrophic velocity derived from sea-surface height (SSH). There is an extensive literature on the analysis of spatiotemporal variance and covariance in different remotely sensed ocean surface datasets such as SSH, SST, and color-derived chlorophyll (see review by O’Brien et al. 2013). Many of these past studies focus on characterizing the propagation behavior of Rossby waves (Chelton and Schlax 1996; Polito and Cornillon 1997; Cipollini et al. 1997; Hill et al. 2000; Cipollini et al. 2001; Polito and Liu 2003; Killworth et al. 2004) and tropical instability waves (Polito et al. 2001; Contreras 2002; Chelton et al. 2000; Lee et al. 2012). The paper by Killworth et al. (2004) is particularly comprehensive and makes a convincing case that a large fraction of the variance in SST and surface chlorophyll arises by advective stirring by the surface geostrophic flow by motions propagating close to the long Rossby wave speed.

Being interested in the wave dynamics themselves, the studies cited above generally em-

70 ployed filters to isolate the spectral bands of interest. Here the approach is slightly different:
 71 we consider the total, unfiltered eddy flux and examine its spectral density in wavenumber,
 72 frequency, and phase-speed space. This perspective is inspired by the atmospheric study of
 73 Randel and Held (1991, henceforth RH91), who made such a diagnosis for the eddy fluxes
 74 of heat and momentum in the troposphere. In particular, presenting the results of the
 75 cross-spectral analysis through 2D contour plots as a function of latitude and phase speed
 76 (or latitude and wavenumber) provides a novel view of the oceanographic data, revealing
 77 the strong latitudinal dependence in the spectra. Our results indicate that the extratropi-
 78 cal meridional eddy heat flux in phase-speed space is indeed concentrated around the long
 79 Rossby-wave phase speed¹. Furthermore, the dominant length scale associated with the
 80 eddy heat flux is everywhere very close to the observed mesoscale eddy diameter. These
 81 conclusions help to explain the success of KA14.

82 In addition to analyzing the satellite data, we perform the same analysis on a state-of-
 83 the-art global eddy-resolving / eddy-permitting ocean model. This comparison serves two
 84 purposes. On one hand, it allows us to probe finer space and time scales than the observations
 85 can resolve. On the other, it provides a form of model validation in the spectral domain.
 86 The broad agreement between the model and the observations is encouraging on both fronts,
 87 suggesting that the observations are sufficient to resolve the dominant scales of eddy heat
 88 transport and that the model shares the spectral characteristics of the observations.

89 Our paper is organized as follows. Sec. 2 describes the satellite data and numerical model
 90 used to obtain SST and SSH. The basic results of the cross-spectral analysis are presented
 91 in Sec. 3 as function of latitude and wavenumber, latitude and frequency, and latitude and
 92 phase speed. In Sec. 4, we calculate the first two moments of the spectra, diagnosing the
 93 dominant scales and also the breadth in wavenumber and phase-speed space, and discuss

¹One slightly confusing yet well documented fact to keep in mind is that coherent nonlinear eddies
 propagate at this phase speed, but larger (apparently linear) Rossby waves propagate somewhat faster
 (Chelton et al. 2007, 2011).

the features observed. Sec. 5 examines the net meridional heat transport in the surface layer and compares the satellite results with the model, and with previous estimates. Conclusions are given in Sec. 6.

2. Data and Models

In order to compute the meridional heat flux, we need concurrent observations of meridional velocity and temperature. We focus our study on a sector in the east Pacific ranging from 180° to 130°W in longitude and spanning 60°S to 50°N longitude. Beyond the intrinsic importance of the eastern Pacific for global climate variability (for example, related to the El Niño / Southern Oscillation phenomenon), this sector was chosen specifically to facilitate comparison between our results and those of KA14 and Abernathey and Marshall (2013). Those earlier works picked this sector because it is relatively statically homogeneous in longitude and contains very little land. These attributes are also well suited to our purposes here, which is to examine the dependence of the spectra on latitude. Understanding the spectral character of eddy fluxes in more inhomogeneous regions, such as western boundary currents, is an important problem but beyond the scope of this work.

a. Sea-Surface Height (SSH)

Sea surface height data is used to estimate surface geostrophic velocities. The altimeter products were produced by SSALTO/DUACS and distributed by AVISO, with support from CNES (<http://www.aviso.oceanobs.com/duacs/>). For this study we use the pre-computed geostrophic velocities derived from the delayed-time, two-satellite “reference” merged sea-level anomaly fields. In these pre-computed velocities, the method of Lagerloef et al. (1999) is applied in the equatorial band ($\pm 5^\circ$). This method, based on the “equatorial geostrophic” vorticity balance, has been validated with *in situ* current meters and allows us to obtain velocity estimates in this region. Nevertheless, we must maintain some skepticism

of the results in the equatorial band; we focus primarily on the extra tropics.

The horizontal spacing of the AVISO gridded data is $1/4^\circ$. The effective resolution of the product is such that it “sees” eddies of approx. 50 km diameter and larger (Chelton et al. 2011); however, smoothing applied during the gridding procedure acts as a low-pass filter, attenuating the signal weakly at wavelengths below 200 km and strongly below 100 km (Ducet et al. 2000). Consequently, the SSH signal displays very little power at short wavelengths (see Fig. 2). This filtering would make it difficult to estimate, for example, spectral slopes characterizing turbulent inertial ranges from the gridded data. However, the focus here is not on the inertial range but of the prominent peak wherein most of the kinetic energy resides (Stammer 1997). This peak, which is everywhere at wavelengths larger than 200 km, is well resolved by the gridded data; mixing-length arguments suggest that these large-scale, highly energetic motions should also dominate the heat flux (Larichev and Held 1995). Directly assessing the contribution of the filtered smaller scales to the heat flux could potentially be explored using along-track satellite or in-situ data, but we do not take that route here. However, one motivation for examining the numerical model (with $1/10^\circ$ resolution, described below) is to attempt to probe smaller scales. In both model and data, we find the heat flux is dominated by wavelengths larger than 200 km, although the model shows a greater contribution from smaller scales.

AVISO produces a map every 7 days which represents a best estimate of the SSH field on that day. The data record begins in 1992, but we only consider the 9.3 year period concurrent with the SST observations, as described below.

b. Sea-Surface Temperature (SST)

The SST data is the Group for High Resolution Sea Surface Temperature (GHRSSST) global Level 4 sea surface temperature analysis produced by the NOAA National Climatic Data Center (Reynolds et al. 2007). An SST map is produced daily on a $1/4^\circ$ grid. We selected the version of the product that blends data from the 4-km Advanced Very High Resolu-

tion Radiometer (AVHRR), the Advanced Microwave Scanning Radiometer-EOS (AMSR-E), and *in situ* ship and buoy observations using optimal interpolation. The SST value represents the temperature at approx. 0.3 m depth. The data coverage for this product begins in June 2002 and ends in Oct. 2011, the period of operation of the AMSR-E instrument. In order to match the temporal resolution of the SSH data, we subsample the SST data on the same days as the AVISO output.

c. 1/10° POP Model

The model analyzed here, a version of the Community Earth System Model (CESM), is described in Small et al. (2014). (The CESM code name for this run is `hybrid_v5_re104_BC5_ne120_t12_pop`) This is a global climate simulation which includes ocean, atmosphere, sea-ice, and land models, similar to that described by McClean et al. (2011). The ocean component, our focus here, uses the Parallel Ocean Program (POP) code and is henceforth referred to as the “POP model.” The POP model has a nominal grid spacing of 0.1° and the atmosphere 0.25° . The two are coupled every six hours. This combination of high-resolution atmosphere, ocean, and coupling results in one of the most realistic global simulations currently available. We consider the use of a coupled model (rather than an ocean-only model) important for simulating the complex air-sea interactions that arise over mesoscale eddies (Small et al. 2008; Bryan et al. 2010), which may influence the eddy heat flux.

We extract daily surface velocity and SST fields from the same sector described above for a five year period (model years 46-50). This is significantly higher temporal resolution than the AVISO data. While higher frequency motions are clearly present in the model spectra, our analysis below indicates that these high frequency (super-weekly) components make a negligible contribution to the meridional heat flux.

Note that we do not attempt to isolate the geostrophic component of the flow in the model; while this would allow for a more direct comparison with the AVISO results, we prefer instead to examine the full eddy flux produced by the model. As we will see, the

similarity between the model and satellite results suggests that the flux in the model is indeed dominated by geostrophic motions.

d. Pre-Processing

Relatively little additional processing is applied to the data, since the observational products we have chosen are already highly processed. We subtract the time mean at each point in space (this is already done in the case of AVISO fields, which are the anomaly relative to 1993-1999 mean), and then the zonal mean at each time step, effectively removing the seasonal cycle and the basin-scale variability. A small amount of smoothing in the frequency domain is also applied before interpolating to phase-speed space (described further below). Everything remaining is included in our definition of “eddy” variability.

e. Coherent Eddy Statistics

A large amount of the variance in midlatitude SSH has been attributed to coherent, nonlinear mesoscale eddies (Chelton et al. 2011). Throughout this study, we compare the length scales and phase speeds that arise from our spectral analysis with the coherent eddy characteristics from the eddy census of Chelton et al. (2011), whose results were made publicly available (<http://cioss.coas.oregonstate.edu/eddies/>). The observed eddy length scale L_s is defined by the average radius of all the eddies at each latitude in the sector. This radius itself is determined for each eddy from the area enclosed by the SSH contour corresponding to the maximum geostrophic flow speed, i.e. where the eddy velocity is greatest. (See Chelton et al. 2011, Sec. 4.2 for further discussion of the eddy length computation.) To convert this length scale to a wavenumber, we follow the recommendation of Chelton et al. (2011) and assume the eddy streamfunction to be described by a gaussian function with an e -folding scale of $\sqrt{2}L_s$. We then define the corresponding eddy wavenumber as $K_{eddy} = (\sqrt{2}L_s)^{-1}$.

Two additional length scales are relevant to our study. The first baroclinic Rossby radius of deformation is a fundamental length scale for the dynamics of large-scale ocean circulation; of particular relevance here is the fact that the most unstable mode of baroclinic instability occurs near the deformation radius (Stammer 1997; Chelton et al. 1998; Scott and Wang 2005; Smith 2007). It also enters into the Rossby wave dispersion relation and exerts a strong control on the observed phase speeds. Following Tulloch et al. (2009) (whose deformation radius data we borrowed), the first baroclinic deformation wavenumber is defined as the largest eigenvalue K_d given by the Sturm-Liouville equation

$$\frac{d}{dz} \left(\frac{f^2}{N^2} \frac{d\Phi}{dz} \right) = -K_d^2 \Phi \quad (1)$$

where f is the Coriolis parameter and N is the Brunt-Väisälä frequency. Our K_d values represent a zonal average over the sector. Given K_d , the long baroclinic Rossby wave phase speed in the zonal direction is then given by

$$c_R = \overline{U}^{zt} - \beta K_d^{-2} \quad (2)$$

where \overline{U}^{zt} is the time- and depth-averaged zonal flow (a Doppler-shift term) and β is the meridional gradient of f . As shown by KA14, polewards of 20° latitude, $c_R \simeq c_{eddy}$ in this sector. We also invoke the Rhines scale, defined as the wavenumber $K_\beta = (\beta/2u_{rms})^{1/2}$, where u_{rms} is the root-mean-square eddy velocity (calculated from the AVISO data). This represents the scale at which turbulent motions become effective at transferring energy into zonally elongated flow such as jets (Rhines 1975; Maltrud and Vallis 1991).

For a given wavenumber K , the wavelength is defined as $L = 2\pi/K$. While elementary, this conversion can be a source of great confusion. For example, under this terminology the Rossby deformation *wavelength* near 45 S is approx. 120 km (as in Tulloch et al. 2009); this is greater than the deformation *radius* of Chelton et al. (1998) by a factor of 2π . It is common to plot wavenumber spectra in terms of “cycles per meter,” which implies the division of wavenumber K by a factor of 2π . This quantity is best described as an “inverse

wavelength,” not a wavenumber. Correct treatment of this issue is crucial, for example, in assessing the strength of the inverse cascade.

3. Cross-Spectral Analysis

Here we describe the technical details of the spectral analysis and present the basic results. Extensive discussion of the results is deferred until Sec. 4.

a. Univariate Power Spectra for SST and Surface Meridional Velocity

Here we describe the calculation of wavenumber-frequency spectra for θ , the SST. (An identical procedure applies to v , the meridional velocity.) In principle, θ is a continuous function of x , zonal coordinate, and t , time: $\theta = \theta(x, t)$ at each latitude φ in the sector. However, our observations are discrete, with N spatial points in longitude (spaced by Δx) and M points in time (spaced by Δt) such that the total zonal length of the sector is $L = N\Delta x$ and the total temporal length of the record is $T = M\Delta t$. The discrete space and time coordinates are denoted as $x_n = n\Delta x$, $t_m = m\Delta t$. For the satellite data used here, $L(\varphi) = 2\pi a \cos(\varphi)(50/360)$ where φ is latitude, $N = 200$, $T = 3402$ days, and $M = 486$.

We write the discrete SST as

$$\theta_{mn} = \theta(x_n, t_m) \quad \{n \mid 0, 1, \dots, N-1\}, \quad \{m \mid 0, 1, \dots, M-1\} . \quad (3)$$

We can express θ_{mn} using a discrete inverse Fourier transform as

$$\theta_{mn} = \frac{\sqrt{2}}{M^2 N^2} \sum_{j=-\frac{M}{2}}^{\frac{M}{2}-1} \sum_{l=0}^{\frac{N}{2}-1} \Theta_{jl} \exp[i(k_l x_n - \omega_j t_m)] \quad (4)$$

where Θ_{jl} are the complex Fourier components, $k_l = 2\pi l/L$ is the wavenumber, and $\omega_j = 2\pi j/T$ is the angular frequency. Equation (4) summarizes the normalization and unit conventions in our Fourier-transform definitions. We adopt the convention of RH91 in which all wavenumbers are positive while frequencies take both positive and negative values. The

values of Θ_{jl} are computed numerically from θ_{mn} using the NumPy implementation of the fast-Fourier-transform (FFT) algorithm.

Parseval's theorem states that the total power of the signal is the same in either basis. The normalization condition chosen in (4) means that each Fourier component represents a fraction of the variance, such that

$$\overline{|\Theta|^2} = \frac{1}{MN} \sum_{m=0}^{M-1} \sum_{n=0}^{N-1} \theta_{mn}^2 = \sum_{j=-\frac{M}{2}}^{\frac{M}{2}-1} \sum_{l=0}^{\frac{N}{2}-1} \Theta_{jl}^* \Theta_{jl} \quad (5)$$

where the asterisk denotes the complex conjugate and the overbar a sum over all wavenumbers / frequencies (here equivalent to a time and zonal mean).

We define the power density as a function of wavenumber as the sum over all frequencies:

$$\overline{|\Theta|^2}(k) = (\Delta k)^{-1} \sum_{j=-\frac{M}{2}}^{\frac{M}{2}-1} \Theta_{jl}^* \Theta_{jl} . \quad (6)$$

The normalization by Δk , the spacing of the discrete wavenumbers, means that $\overline{|\Theta|^2}(k)$ represents a continuous power density function, giving results which are independent of N . Similarly, we define the power density as a function of frequency as the sum over wavenumbers,

$$\overline{|\Theta|^2}(\omega) = (\Delta \omega)^{-1} \sum_{l=0}^{N-1} \Theta_{jl}^* \Theta_{jl} \quad (7)$$

where $\Delta \omega$ is the spacing of the discrete frequencies.

As in RH91, we construct phase speed spectra by interpolating the spectral density from (k, ω) space to (k, c) space, where $c = \omega/k$ is the phase speed. Before interpolating, the density $(\Delta \omega)^{-1} \Theta_{jl}^* \Theta_{jl}$ must be multiplied by k ; this transformation ensures that the total power is the same whether integrating over ω or c . We also smooth the signal in frequency space before interpolating using a Gaussian filter with an e -folding scale of two frequency bands. We interpolate to 1000 points in c , evenly spaced from -1 to 1 m s⁻¹ in order to capture the wide range of phase speeds with high precision. After summing over wavenumbers, we obtain the power density as a function of phase speed, $\overline{|\Theta|^2}(c)$.

Raw wavenumber-frequency power spectra at different locations in the ocean are shown in numerous other publications (e.g. Killworth et al. 1997; Wunsch 2010; Wortham and Wunsch 2014) and are not plotted here. Here we are interested instead in the integrals of the spectra. In Fig. 1 we plot $|\overline{\Theta}|^2(\varphi, k)$, $|\overline{\Theta}|^2(\varphi, \omega)$, and $|\overline{\Theta}|^2(\varphi, c)$, using a logarithmic color scale. This figure reveals the distribution of SST variance by wavenumber, frequency, and phase speed as a function of latitude.

From the surface meridional velocity data, we define v_{mn} (the space/time data) and V_{jl} (the Fourier transform) in the same way described above. Fig. 2 shows $|\overline{V}|^2(\varphi, k)$, $|\overline{V}|^2(\varphi, \omega)$, and $|\overline{V}|^2(\varphi, c)$.

b. Eddy Heat Flux Cross Spectra

Parseval's theorem also applies to the product of θ and v ; the eddy heat flux is the same whether expressed as an average of space / time components or a sum of Fourier components. We express this mathematically as

$$\overline{V\Theta} = \frac{1}{MN} \sum_{m=0}^{M-1} \sum_{n=0}^{N-1} v_{mn} \theta_{mn} = \sum_{j=-\frac{M}{2}}^{\frac{M}{2}-1} \sum_{l=0}^{\frac{N}{2}-1} \Re\{V_{jl}^* \Theta_{jl}\} . \quad (8)$$

Just as described above for the univariate spectra, we can sum the components of $\Re\{V_{jl}^* \Theta_{jl}\}$ selectively to define $\overline{V\Theta}(\varphi, k)$, $\overline{V\Theta}(\varphi, \omega)$, and $\overline{V\Theta}(\varphi, c)$. These functions are plotted in Fig. 3. Unlike the power spectra described above $\overline{V\Theta}$ can take both positive and negative values, corresponding to northward and southward heat transport. As seen in Fig. 3, the eddy heat flux is poleward in both hemispheres, except near the equator, where it reverses. This is consistent with the mean SST gradient, which also reverses near the equator; the eddy flux is always down gradient. Further discussion and comparison of the spectra is deferred until Sec. 4.

280 The analysis of the model is identical. Only the spatiotemporal sampling and resolution
 281 are different. For the model L , the sector width is the same, $N = 500$, $T = 1825$ days, and
 282 $M = 1825$. The different spectra from the POP model are shown in Figs. 4, 5, and 6. To
 283 facilitate comparison in phase-speed space, which is the primary focus of our study, in Fig. 7
 284 we plot $\overline{V\Theta}(c)$ from both satellite data and POP model in the same figure. Showing only
 285 the extratropics (poleward of 10°) in Fig. 7, where the magnitude of the phase speed is small
 286 compared to the equatorial region, allows us to examine the spectra in closer detail.

287 4. Spectral Moments and Discussion

288 While a visual comparison of the spectra in Figs. 1-7 is informative, a more quantitative
 289 comparison is desirable. In particular, we wish to assess whether the spectra peak in the same
 290 locations and how those peaks are related to the underlying dynamics. Furthermore, we wish
 291 to assess to what extent the spectra are narrowly concentrated around these peaks, versus
 292 broadly distributed. In this section we characterize the properties of the power spectra and
 293 cross spectra via their moments in wavenumber, frequency, and phase speed space. The first
 294 moment tells us about the dominant scale. The second moment tells us how concentrated
 295 the distribution is about that scale. Spectral moments play an important role in the theory
 296 of geostrophic turbulence and have frequently been used to characterize the length scales of
 297 ocean eddies (e.g. Rhines 1975; Scott and Wang 2005; Tulloch et al. 2011).

298 We define the first moment of a wavenumber spectrum $\overline{|\Theta|^2}(k)$ at a given latitude (itself
 299 defined in 6) as

$$M_1^k(\overline{|\Theta|^2}) = \frac{\int k \overline{|\Theta|^2}(k) dk}{\int \overline{|\Theta|^2}(k) dk} \quad (9)$$

300 where the integrals are performed over all wavenumbers. The second moment is then defined

$$M_2^k(\overline{|\Theta|^2}) = \frac{\int (k - M_1^k)^2 \overline{|\Theta|^2}(k) dk}{\int \overline{|\Theta|^2}(k) dk} . \quad (10)$$

302 We make analogous definitions for the ω and c moments, and also for the moments of the
 303 other spectra $\overline{|V|^2}$ and $\overline{V\Theta}$.

304 For a gaussian distribution, M_1 is the mean and M_2 is the variance. The interpretation of
 305 M_1 and M_2 is therefore most clear when the spectra have a clearly defined, dominant peak.
 306 In the case of $\overline{V\Theta}$, which is not positive definite, it is possible for the normalization factor in
 307 the denominator of (9) and (10) to approach zero, leading to a meaningless result. To avoid
 308 this situation, we mask the moments at latitudes where the ratio $|\int \overline{V\Theta}| / \int |\overline{V\Theta}| < 0.9$.
 309 This is only the case in regions where the mean SST gradient is weak (primarily near 15°S)
 310 and the heat flux is vanishingly small and noisy. At most latitudes, the heat flux does display
 311 a clear spectral peak, as evident in Figs. 3 and 6.

312 The first moments $M_1^k(\overline{|\Theta|^2})$, $M_1^k(\overline{|V|^2})$, and $M_1^k(\overline{V\Theta})$ are plotted in the upper panel of
 313 Fig. 8, with the second moments $M_2^k(\overline{|\Theta|^2})$, $M_2^k(\overline{|V|^2})$, and $M_2^k(\overline{V\Theta})$ in the middle panel, for
 314 both the satellite data and the POP model. The c moments are in shown in Fig. 9. Equipped
 315 with this more quantitative description, we are now prepared to discuss the features and
 316 characteristics of the spectra.

317 At all latitudes, the first moment of the of the eddy heat flux $\overline{V\Theta}(k)$ is at wavelengths of
 318 250km or greater (Fig. 8). Generally speaking, these are the same wavelengths containing
 319 most of the kinetic energy (as indicated by $\overline{|V|^2}(k)$). The dominance of these wavelengths
 320 in the kinetic energy has been noted by other authors (e.g. Wunsch 2010; Wortham and
 321 Wunsch 2014) and has been attributed to a weak geostrophic-turbulent inverse cascade of
 322 energy from some source scale to the deformation radius (Stammer 1997; Arbic and Flierl
 323 2004; Scott and Wang 2005; Tulloch et al. 2011). It is interesting, although unsurprising, to
 324 see that these wavelengths also dominate the heat flux.

325 To further analyze the dominant scales of the heat transport, the bottom panel of Fig. 8
 326 plots the ratio the three important wavenumbers identified in Sec. 2 (the coherent eddy

327 wavenumber K_{eddy} , the deformation wavenumber K_d , and the Rhines wavenumber K_β) and
 328 $M_1^k(\overline{V\Theta})$. This ratio is very close to one for K_{eddy} polewards of 20° . The consistent propor-
 329 tionality between the dominant length scale of the heat flux and the diameter of coherent
 330 mesoscale eddies strongly suggests that the mesoscale eddies are responsible for most of the
 331 heat transport. The deformation wavenumber is consistently larger than $M_1^k(\overline{V\Theta})$, especially
 332 at high latitudes, where the ratio approaches 4. The Rhines wavenumber is smaller.

333 Of course, when interpreting the wavenumber spectra, we must keep in mind the low-
 334 pass-filtering effect of the AVISO processing, which artificially attenuates small scales. This
 335 filtering attenuates the inertial range at wavelengths below 200 km (Ducet et al. 2000), in
 336 which power-law dependence is observed in the along-track altimetry (Xu and Fu 2012).
 337 One probable consequence of this filtering is to bias $M_1^k(|\overline{V}|^2)$ towards larger length scales.
 338 This effect can be seen by comparing with the POP results. It is clear from Figs. 1-7 that
 339 there is significantly more small-scale variance in the POP fields. This is certainly reflected
 340 in larger values of M_2^k (Fig. 8) for the POP model by a factor of 2-3 for all three spectra.
 341 The values of $M_1^k(|\overline{\Theta}|^2)$ are also significantly different between the POP model and the
 342 data; a dominance of shorter wavelengths is seen in the model SST. Since the SST spectra
 343 are red throughout (in contrast with the energy spectra, which contain a clear peak), such a
 344 shift is expected. There is also a shift to shorter wavelengths in the POP $M_1^k(|\overline{V}|^2)$ and
 345 $M_1^k(\overline{V\Theta})$; however, the magnitude of the shift is much smaller (generally less than 20%), and
 346 at many latitudes, the model and data coincide well. This indicates that the first moment
 347 of $\overline{V\Theta}(k)$ is primarily determined by the mesoscale peak in $V^2(k)$ and only weakly affected
 348 by higher wavenumbers where the energy typically falls off as a power law in k .

349 We now turn to the phase speed moments in Fig. 9. In general, the first moments of
 350 the eddy heat transport $M_1^c(\overline{V\Theta})$ tracks $M_1^c(|\overline{V}|^2)$ in both the model and data, especially
 351 poleward of about 10° latitude. Moreover, this moment tracks quite closely the observed
 352 eddy phase speed c_{eddy} , which itself is well described by the long Rossby wave phase speed
 353 c_R poleward of 20° latitude (Tulloch et al. 2009; Klocker and Abernathey 2014). This

further suggests that the extratropical heat flux is generated through mixing by coherently propagating eddies. Closer to the equator the moments are more noisy due to regions of vanishing temperature gradient and heat flux. Nevertheless, the heat flux and energy spectral moments are consistent with tropical instability waves, which propagate at speeds of 0.3-0.4 m s⁻¹ (see also Contreras 2002; Polito et al. 2001). In general, the first moments of the temperature spectra $M_1^c(|\overline{\Theta}|^2)$ tend towards slower phase speeds in both model and data, reflecting a wider range of mechanisms which cause temperature variance.

In the second moments show that the temperature variance (in both model and data) is spread much more widely across phase speeds than either the velocity variance or the heat flux. For the satellite data, both $M_2^c(|\overline{V}|^2)$ and $M_2^c(\overline{V\Theta})$ have values of $< (0.05 \text{ m s}^{-1})^2$ in the extratropics, indicating that the corresponding phase speed spectra are highly peaked about their first moment. This result provides an answer to one of our key motivating questions; given this narrow peak, the success of the monochromatic model of KA14 in the extratropics seems unsurprising; there is clearly a single dominant phase speed in the data. However, the model moments indicate somewhat greater spread in phase speed, a fact not immediately evident in Fig. 7 on visual inspection. As with the wavenumber moments, $M_2^c(|\overline{\Theta}|^2)$ is uniformly higher in the model than in the data. In contrast to the wavenumber spectra, the temperature data actually contains *more* phase-speed spread than the model.

5. Net Meridional Heat Transport and Eddy Diffusivity

In this section we consider the total meridional eddy heat transport at each latitude. This section has two goals. First, we demonstrate that our “direct” method of estimating near-surface heat transport from satellite data provides results that are consistent, in magnitude and spatial structure, with previous model-based estimates. Secondly, we demonstrate that the differences in heat transport between the POP model and AVISO data can be explained through the lens of the Ferrari and Nikurashin (2010) diffusivity closure.

We calculate the net meridional eddy heat transport from both the satellite data and POP model. This heat transport is defined as

$$\mathcal{H} = \rho_0 c_p h \overline{v'\theta'} \quad (11)$$

where $\rho_0 = 1027 \text{ kg m}^{-3}$ is a reference density and $c_p = 4186 \text{ J K}^{-1} \text{ kg}^{-1}$ is the specific heat of seawater. In order to translate the surface eddy temperature flux $\overline{v'\theta'}$ into a heat flux, it must be multiplied by a finite depth h . This choice of depth strongly influences the estimate of \mathcal{H} . We opt for a lower bound estimate.

We expect that the remotely sensed surface velocities and temperatures are representative of the mixed layer. Observational studies have shown the the vertical amplitude of eddy heat transport in the subtropical North Pacific is maximum near the surface and decays to zero over a depth scale of several hundred meters (Roemmich and Gilson 2001; Qiu and Chen 2005). Since our surface observations cannot asses the subsurface component with any confidence, we simply present them as a lower bound on the vertically integrated heat transport. Based on the Argo-derived mixed-layer estimates of this sector from Holte and Talley (2009), we use a spatially constant value of $h = 50 \text{ m}$. This is itself a lower bound; in the Southern Ocean, the annual mean mixed layer is considerably deeper. Furthermore, mixed layer depth exhibits considerable temporal variability. However, a spatially constant value facilitates direct comparison between the model and the data, which is more important here than the precise magnitude of \mathcal{H} .

The value of \mathcal{H} is shown in Fig. 10 for both satellite data and POP model, normalized to give units of TW (10^{12} W) per degree of longitude. The order of magnitude in the extra-tropics is roughly 0.1 - 0.3 TW per degree, or 10-30 TW across the roughly 100 degree width of the Pacific. For comparison, Jayne and Marotzke (2002) estimate 50-100 TW in the upper 25m of the global ocean (their Fig. 3). Of course, the heat transport is not zonally homogeneous across the Pacific, with transport typically concentrated in the western boundary current regions. The point is that the present eddy heat transport estimates are of the same order of magnitude of other estimates (Jayne and Marotzke 2002; Volkov et al.

2008; Dong et al. 2014), and therefore represent a significant contribution to the total global meridional heat transport. The meridional structure is also similar to the studies cited.

The model and data generally agree quite well, both in spatial structure and magnitude of \mathcal{H} . Disagreement in magnitude, by factors of 2-3, arises in two principal locations: near the equator and in the ACC. (This disagreement is also visible, though not quite as obvious, in comparing Figs. 3 and 6.) In these areas, the model produces a larger eddy heat transport. What is the physical origin of this disagreement? The closure model of Ferrari and Nikurashin (2010) posits that the eddy flux depends on four principal factors: the background meridional tracer gradient, the eddy kinetic energy (EKE), the eddy size, and the eddy phase speed relative to the mean flow. Using kinematic simulations of passive tracer advection, KA14 verified that such a model can accurately describe eddy fluxes in this sector. While we do not attempt to quantitatively fit that model in this study, it is instructive to consider these different factors when comparing the model with the data. Figs. 8 and 9 suggest that the dominant length scales and phase speeds in the model and data are very similar. Therefore, we can expect the differences in \mathcal{H} to be due to differences in background meridional temperature gradient and eddy kinetic energy.

In Fig. 10b, we plot the time and zonal mean meridional SST gradient $\partial\bar{\theta}/\partial y$ from the model and the data. We see that the gradients are nearly identical, except in the equatorial region, where the model gradients can be 50% larger. This partly explains the fact that the model \mathcal{H} is higher in this region. The EKE, defined as $0.5(\overline{v'^2} + \overline{u'^2})$, is plotted in Fig. 10c. (Technically only v' enters directly in the meridional flux, but the eddy velocities are relatively isotropic in the extratropics.) The model and data EKE are quite similar in the extratropics, but differ significantly at low latitudes and in the ACC. The model is uniformly more energetic, by a factor of two in the ACC and at the equator; the regions of EKE mismatch are the same as those of differing eddy heat flux. Therefore, we can also attribute some of the discrepancy in heat transport to the discrepancy in EKE.

Finally, we plot the surface eddy diffusivity for heat, defined as

$$D = -\overline{v'\theta'} / \frac{\partial \bar{\theta}}{\partial y} . \quad (12)$$

Where the gradient vanishes, D blows up. To avoid this, we mask D wherever the absolute value of the gradient is less than one tenth of its global mean value. This occurs in different locations for model and data, making a direct comparison in the equatorial region difficult. Nevertheless, the differences observed in EKE are clearly reflected in D as well. Moreover, the general pattern in D , low at high latitudes and high at low latitudes, is very consistent with KA14. That study examined the eddy diffusivity of a synthetic passive tracer advected by the AVISO velocity fields. The similarity in the magnitude and spatial structure of D between this study and that one suggests that the eddy heat flux is generated through advection of the mean temperature gradient by the geostrophic eddy field.

6. Conclusions

This study was largely motivated by KA14, who found that the extratropical eddy flux of a simulated passive tracer in this sector could be parameterized in terms of a single wavenumber and phase speed at each latitude. How can such a monochromatic model be compatible with the broadband variability of the ocean? To resolve this contradiction, we examined the surface eddy heat flux directly using satellite products. We calculated the wavenumber frequency power spectrum at each latitude for surface geostrophic velocity and SST as well as the cross spectrum of these two fields. We integrated these spectra at constant wavenumber, frequency, and phase speed in order to form Figs. 1-7. To quantify the dominant scales and the breadth of their distribution in spectral space, we computed first and second spectral moments. We also performed the same analysis on a high-resolution coupled climate model.

We found that, poleward of 20° , the dominant length scale for both velocity and heat flux is very close to the scale of the nonlinear coherent mesoscale eddies identified by Chelton

et al. (2011). For the data, the spectral breadth in wavenumber space, as characterized by the second moment, is between 1 and 2 cycles per 1000 km. For the model, the spectral breadth was greater by about a factor of two. This probably reflects the fact that the AVISO data is attenuated at scales below 200 km, resulting in narrower spectra.

Similarly, poleward of 20° , the dominant phase speed for both velocity and heat flux is very close to the propagation speed of tracked nonlinear coherent mesoscale eddies. As shown by KA14 and Tulloch et al. (2009), this speed is approximately equal to c_R (eq. 2), the long Rossby wave phase speed. The spectral breadth in phase-speed space is approx. 5 cm s^{-1} for the data. The model spectral breadth is again greater by a factor of two or more. Taken together with the wavenumber spectra, these results indicate that the eddy heat flux is generated predominantly by the coherent eddies observed by Chelton et al. (2011).

KA14 reached the same conclusion through a very different approach. They performed kinematic advection-diffusion experiments on a passive tracer driven by AVISO velocity fields and attempted to fit the model of Ferrari and Nikurashin (2010) to the resulting eddy diffusivities. The best agreement was found using the coherent eddy length scale together with the coherent eddy phase speed—the exact same scales which emerged from the present spectral analysis.

Both these studies are primarily diagnostic, emphasizing the importance of coherent eddy kinetic energy, size and phase speed in determining eddy fluxes. They do not explain *why* the eddies have the energy, size, and phase speed that they do. Each of these topics comprises an active field of research. The main energy source for mesoscale eddies is the baroclinic instability of the large-scale density field (Gill et al. 1974; von Storch et al. 2012). However, in order to explain the magnitude of the equilibrated eddy kinetic energy, one must also understand how the eddy energy is dissipated, a far less obvious question (Cessi 2008; Arbic et al. 2009; Ferrari and Wunsch 2010; Abernathey et al. 2011). Similarly, for the length scales, there is a general belief in the existence of a weak inverse energy cascade in the ocean which transfers energy from a source near the deformation radius to the moderately

larger observed scales (Scott and Wang 2005; Tulloch et al. 2011). However, it is far from clear what *halts* this cascade; proposed mechanisms invoke the importance of β (via Rhines-scale arguments) and also the role of friction (Held and Larichev 1996; Smith et al. 2002; Lapeyre and Held 2003; Thompson and Young 2006, 2007). The theoretical explanation for the observed eddy propagation speed also remains an active topic of debate (Killworth et al. 1997; Chelton et al. 2007, 2011; Wortham and Wunsch 2014). Progress on any of these topics would lead directly to progress on the eddy parameterization problem.

One clear shortcoming of the approach used here, which is constrained by the satellite data, is that it does not address the sub-surface. Although eddy energy and flux peak near the surface, significant energy and transport exist at depth, particularly in the Southern Ocean. Many methods have recently been proposed to extrapolate satellite data into the interior (Lapeyre and Klein 2006; Isern-Fontanet et al. 2008; Scott and Furnival 2012; Wang et al. 2013; Smith and Vanneste 2013). Future studies could attempt to take advantage of such methods to calculate the cross spectra of subsurface eddy heat fluxes. Novel methods have been applied to estimate subsurface eddy heat transport from Argo data (Dong et al. 2014), but such methods are unlikely to yield results in the spectral domain.

Finally, the inconclusive nature of our findings in the equatorial region is a clear call for further study. The eddy heat flux here is dominated not by mesoscale eddies but by much larger tropical instability waves (Jochum and Murtugudde 2006). The model and data disagree significantly near the equator. This is likely due in part to the difficulty of reconstructing equatorial currents from SSH data alone, but model biases cannot be ruled out either. Furthermore, the vanishingly weak SST gradients result in weak, noisy heat fluxes. KA14 also noted that the Ferrari and Nikurashin (2010) theory did not fare well in the equatorial region. Therefore, a deeper understanding of how tropical instability waves mix and transport heat in this climatically important region should be a top priority.

Acknowledgments.

R. Abernathey gratefully acknowledges support by NASA ROSES grant no. NNX14AI46G.

REFERENCES

- 512 Abernathey, R., J. Marshall, and D. Ferreira, 2011: The dependence of Southern Ocean
513 meridional overturning on wind stress. *J. Phys. Oceanogr.*, **41** (**12**), 2261–2278.
- 514 Abernathey, R., J. Marshall, E. Shuckburgh, and M. Mazloff, 2010: Enhancement of
515 mesoscale eddy stirring at steering levels in the Southern Ocean. *J. Phys. Oceanogr.*,
516 **40**, 170–185.
- 517 Abernathey, R. and J. C. Marshall, 2013: Global surface eddy diffusivities derived from
518 satellite altimetry. *J. Geophys. Res.*, **118**, 901–916.
- 519 Abernathey, R. P. and P. Cessi, 2014: Topographic enhancement of eddy efficiency in baro-
520 clinic equilibration. *J. Phys. Oceanogr.*, **44**, 2107–2126.
- 521 Arbic, B. K. and G. R. Flierl, 2004: Baroclinically unstable geostrophic turbulence in the
522 limits of strong and weak bottom Ekman friction: Application to midocean eddies. *J. Phys.*
523 *Oceanogr.*, **34**, 2257–2274.
- 524 Arbic, B. K., et al., 2009: Estimates of bottom flows and bottom boundary layer dissipation
525 of the oceanic general circulation from global high-resolution models. *J. Geophys. Res.*,
526 **114**, C02024.
- 527 Bryan, F. O., R. Tomas, J. M. Dennis, D. B. Chelton, N. G. Loeb, and J. L. McClean,
528 2010: Frontal scale air-sea interaction in high-resolution coupled climate models. *Journal*
529 *of Climate*, **23**.
- 530 Cessi, P., 2008: An energy-constrained parameterization of eddy buoyancy flux. *J. Phys.*
531 *Oceanogr.*, **38**, 1807–1820.

Chelton, D. B., R. A. de Szoeke, M. G. Schlax, K. Naggar, and N. Siwertz, 1998: Geographical variability of the first baroclinic Rossby radius of deformations. *J. Phys. Oceanogr.*, **28**, 433–450.

Chelton, D. B. and M. G. Schlax, 1996: Global observations of oceanic Rossby waves. *Science*, **272** (5259), 234–238.

Chelton, D. B., M. G. Schlax, and R. M. Samelson, 2011: Global observations of nonlinear mesoscale eddies. *Progress in Oceanography*, **91**, 167–216.

Chelton, D. B., M. G. Schlax, R. M. Samelson, and R. A. de Szoeke, 2007: Global observations of large oceanic eddies, submitted to GRL.

Chelton, D. B., F. J. Wentz, C. L. Gentemann, R. A. de Szoeke, and M. G. Schlax, 2000: Satellite microwave SST observations of transequatorial tropical instability waves. *Geophys. Res. Lett.*, **27** (9), 1239–1242.

Cipollini, P., D. Cromwell, P. G. Challenor, and S. Raffaglio, 2001: Rossby waves detected in global ocean colour data. *Geophys. Res. Lett.*, **28** (2), 323–326.

Cipollini, P., D. Cromwell, M. S. Jones, G. D. Quartly, and P. G. Challenor, 1997: Concurrent altimeter and infrared observations of Rossby wave propagation near 34°N in the northeast Atlantic. *Geophys. Res. Lett.*, **24** (8), 889–892.

Contreras, R. F., 2002: Long-term observations of tropical instability waves. *J. Phys. Oceanogr.*, **32**, 2715–2722.

Dong, C., J. C. McWilliams, Y. Liu, and D. Chen, 2014: Global heat and salt transports by eddy movement. *Nature Comm.*, **5** (3294).

Ducet, N., P. Y. Le Traon, and G. Reverdin, 2000: Global high-resolution mapping of ocean circulation from TOPEX/Poseidon and ERS-1 and -2. *J. Geophys. Res.*, **105** (CH), 19,477–19,498.

556 Ferrari, R. and M. Nikurashin, 2010: Suppression of eddy diffusivity across jets in the
557 Southern Ocean. *J. Phys. Oceanogr.*, **40**, 1501–1519.

558 Ferrari, R. and C. Wunsch, 2010: The distribution of eddy kinetic and potential energies in
559 the global ocean. *Tellus*, **62A**, 92–108.

560 Gill, A. E., J. S. A. Green, and A. J. Simmons, 1974: Energy partition in the large-scale
561 ocean circulation and the production of mid-ocean eddies. *J. Marine Res.*, **21**, 499–528.

562 Held, I. M. and V. D. Larichev, 1996: A scaling theory for horizontally homogeneous, baro-
563 clinically unstable flow on a beta plane. *J. Atmos. Sci.*, **53** (7), 946–953.

564 Hill, K. L., I. S. Robinson, and P. Cipollini, 2000: Propagation characteristics of extratropical
565 planetary waves observed in the atsr global sea surface temperature record. *J. Geophys.*
566 *Res.*, **105** (C9), 21 927–21 945.

567 Holloway, G., 1986: Estimation of oceanic eddy transports from satellite altimetry. *Nature*,
568 **323**, 343–344.

569 Holte, J. and L. Talley, 2009: A new algorithm for finding mixed layer depths with applica-
570 tions to Argo data and Subantarctic Mode Water formation. *J. Atm. Ocean. Tech.*, **26**,
571 1920–1939.

572 Hughes, C. W. and S. D. Williams, 2010: The color of sea level: Importance of spatial
573 variations in spectral shape for assessing the significance of trends. *Journal of Geophysical*
574 *Research: Oceans (1978–2012)*, **115** (C10).

575 Isern-Fontanet, J., G. Lapeyre, P. Klein, B. Chapron, and M. W. Hecht, 2008: Three-
576 dimensional reconstruction of oceanic mesoscale currents from surface information. *J.*
577 *Geophys. Res.*, **113**, C09 005.

578 Jayne, S. R. and J. Marotzke, 2002: The oceanic eddy heat transport. *J. Phys. Oceanogr.*,
579 **32**, 3328–3345.

580 Jochum, M. and R. Murtugudde, 2006: Temperature advection by tropical instability waves.
581 *Journal of Physical Oceanography*, **36** (4), 592–605.

582 Keffer, T. and G. Holloway, 1988: Estimating Southern Ocean eddy flux of heat and salt
583 from satellite altimetry. *Nature*, **332**, 624 – 626.

584 Killworth, P. D., D. B. Chelton, and R. A. de Szoeke, 1997: The speed of observed and
585 theoretical long extratropical planetary waves. *J. Phys. Oceanogr.*, **27**, 1946–1966.

586 Killworth, P. D., P. Cipollini, B. M. Uz, and J. R. Blundell, 2004: Physical and biological
587 mechanisms for planetary waves observed in satellite-derived chlorophyll. *J. Geophys. Res.*,
588 **109**, C07 002.

589 Klocker, A. and R. Abernathey, 2014: Global patterns of mesoscale eddy properties and
590 diffusivities. *J. Phys. Oceanogr.*, **44**, 1030–1047.

591 Klocker, A., R. Ferrari, and J. H. LaCasce, 2012a: Estimating suppression of eddy mixing
592 by mean flow. *J. Phys. Oceanogr.*, **9**, 1566–1576.

593 Klocker, A., R. Ferrari, J. H. LaCasce, and S. T. Merrifield, 2012b: Reconciling float-based
594 and tracer-based estimates of eddy diffusivities. *J. Marine Res.*, **70** (4), 569–602.

595 Lagerloef, G., G. Mitchum, R. Lukas, and P. Niiler, 1999: Tropical Pacific near-surface
596 currents estimated from altimeter, wind and drifter data. *J. Geophys. Res.*, **104**, 313–23.

597 Lapeyre, G. and I. M. Held, 2003: Diffusivity, kinetic energy dissipation, and closure theories
598 for the poleward eddy heat flux. *J. Atmos. Sci.*, **60**, 2907–2917.

599 Lapeyre, G. and P. Klein, 2006: Dynamics of the upper oceanic layers in terms of surface
600 quasigeostrophy theory. *Journal of physical oceanography*, **36** (2), 165–176.

601 Larichev, V. D. and I. M. Held, 1995: Eddy amplitudes and fluxes in a homogeneous model
602 of fully developed baroclinic instability. *J. Atmos. Sci.*, **25**, 2285–2297.

603 Lee, T., G. Lagerloef, M. M. Gierach, H.-Y. Kao, S. Yueh, and K. Dohan, 2012: Aquarius
604 reveals salinity struture of tropical instability waves. *Geophys. Res. Lett.*, **39**, L12 610.

605 Maltrud, M. and G. Vallis, 1991: Energy spectra and coherent structures in forced two-
606 dimensional and beta-plane turbulence. *Journal of Fluid Mechanics*, **228**, 321–342.

607 Marshall, J., E. Shuckburgh, H. Jones, and C. Hill, 2006: Estimates and implications of
608 surface eddy diffusivity in the Southern Ocean derived from tracer transport. *J. Phys.*
609 *Oceanogr.*, **36**, 1806–1821.

610 McClean, J. L., et al., 2011: A prototype two-decade fully-coupled fine-resolution ccsm
611 simulation. *Ocean Modelling*, **39**, 10–30.

612 O’Brien, R. C., P. Cipollini, and J. R. Blundell, 2013: Manifestation of oceanic rossby waves
613 in long-term multiparametric satellite datasets. *Remote Sensing of Environment*, **129**,
614 111–121.

615 Polito, P. S. and P. Cornillon, 1997: Long baroclinic rossby waves detected by
616 topex/poseidon. *J. Geophys. Res.*, **102 (C2)**, 3215–3235.

617 Polito, P. S. and W. T. Liu, 2003: Global characterization of Rossby waves at several spectral
618 bands. *J. Geophys. Res.*, **108 (C1)**, 3018.

619 Polito, P. S., J. P. Ryand, W. T. Liu, and F. P. Chavez, 2001: Oceanic and atmospheric
620 anomalies of tropical instability waves. *Geophys. Res. Lett.*, **28 (11)**, 2233–2236.

621 Prandtl, L., 1925: Bericht untersuchungen zur ausgebildeten turbulenz. *Zs. angew. Math.*
622 *Mech.*, **5**, 136–139.

623 Qiu, B. and S. Chen, 2005: Eddy-induced heat transport in the subtropical North Pacific
624 from Argo, TMI, and altimetry measurements. *J. Phys. Oceanogr.*, **35**, 458–473.

625 Randel, W. J. and I. M. Held, 1991: Phase speed spectra of transient eddy fluxes and critical
626 layer absorption. *J. Atmos. Sci.*, **48**, 688–697.

627 Reynolds, R. W., T. M. Smith, C. Liu, D. B. Chelton, K. S. Casey, and M. G. Schlax,
 628 2007: Daily high-resolution-blended analyses for sea surface temperature. *J. Climate*, **20**,
 629 5473–5491.

630 Rhines, P., 1975: Waves and turbulence on a beta-plane. *J. Fluid Mech.*, **69**, 417–433.

631 Richman, J. G., C. Wunsch, and N. G. Hogg, 1977: Space and time scales of mesoscale
 632 motion in the western north atlantic. *Reviews of Geophysics*, **15** (4), 385–420.

633 Roemmich, D. and J. Gilson, 2001: ddy transport of heat and thermocline waters in the
 634 North Pacific: a key to interannual/decadal climate variability? *J. Phys. Oceanogr.*, **31**,
 635 675–687.

636 Scott, R. B. and D. G. Furnival, 2012: Assessment of traditional and new eigenfunction bases
 637 applied to extrapolation of surface geostrophic current time series to below the surface in
 638 an idealized primitive equation simulation. *J. Phys. Oceanogr.*, **42**, 65–178.

639 Scott, R. B. and F. Wang, 2005: Direct evidence of an oceanic inverse kinetic energy cascade
 640 from satellite altimetry. *J. Phys. Oceanogr.*, **35**, 1650–1666.

641 Small, R., et al., 2008: Air–sea interaction over ocean fronts and eddies. *Dynamics of At-*
 642 *mospheres and Oceans*, **45** (3), 274–319.

643 Small, R. J., et al., 2014: A new synoptic scale resolving global climate simulation using the
 644 Community Earth System Model. *J. Adv. Modeling Earth Systems*.

645 Smith, K. S., 2007: The geography of linear baroclinic instability in the earth’s oceans. *J.*
 646 *Marine Res.*, **65**, 655–683.

647 Smith, K. S., G. Boccaletti, C. C. Henning, I. Marinov, C. Y. Tam, I. M. Held, and G. K.
 648 Vallis, 2002: Turbulent diffusion in the geostrophic inverse cascade. *J. Fluid Mech.*, **469**,
 649 13–48.

650 Smith, K. S. and J. Marshall, 2009: Evidence for enhanced eddy mixing at mid-depth in the
651 Southern Ocean. *J. Phys. Oceanogr.*, **39**, 50–69.

652 Smith, K. S. and J. Vanneste, 2013: A surface-aware projection basis for quasigeostrophic
653 flow. *J. Phys. Oceanogr.*, **43**, 548–562.

654 Stammer, D., 1997: Global characteristics of ocean variability estimated from regional
655 TOPEX/ POSEIDON altimeter measurements. *J. Phys. Oceanogr.*, **27**, 1743–1769.

656 Stammer, D., 1998: On eddy characteristics, eddy transports, and mean flow properties. *J.*
657 *Phys. Oceanogr.*, **28**, 727–739.

658 Taylor, G. I., 1915: Eddy motion in the atmosphere. *Philosophical Transactions of the Royal*
659 *Society A*, **215**, 1–26.

660 Thompson, A. F. and W. R. Young, 2006: Scaling baroclinic eddy fluxes: Vortices and
661 energy balance. *J. Phys. Oceanogr.*, **36**, 720–738.

662 Thompson, A. F. and W. R. Young, 2007: Two-layer baroclinic eddy heat fluxes: Zonal
663 flows and energy balance. *J. Atmos. Sci.*, **64**, 3214–3232.

664 Trenberth, K. E. and J. M. Caron, 2001: Estimates of meridional atmosphere and ocean
665 heat transports. *J. Climate*, **14**, 3433–3443.

666 Tulloch, R., J. Marshall, C. Hill, and K. S. Smith, 2011: Scales, growth rates, and spectral
667 fluxes of baroclinic instability in the ocean. *J. Phys. Oceanogr.*, **31**, 1057–1076.

668 Tulloch, R., J. Marshall, and K. S. Smith, 2009: Interpretation of the propagation of sur-
669 face altimetric observations in terms of planetary waves and geostrophic turbulence. *J.*
670 *Geophys. Res.*, **114**, C02005.

671 Visbeck, M., J. Marshall, and T. Haine, 1997: Specification of eddy transfer coefficients in
672 coarse-resolution ocean circulation models. *J. Phys. Oceanogr.*, **27**, 381–403.

673 Volkov, D., T. Lee, and L. Fu, 2008: Eddy-induced meridional heat transport in the ocean.
674 *Geophys. Res. Lett.*, **35**, L20 601.

675 von Storch, J., C. Eden, I. Fast, H. Haak, D. Hernandez-Deckers, E. Maier-Reimer,
676 J. Marotzke, and D. Stammer, 2012: An estimate of lorenz energy cycle for the world
677 ocean based on the 1/10° storm/ncp simulation. *J. Phys. Oceanogr.*, **42**, 2185–2205.

678 Wang, J., G. R. Flierl, J. H. LaCasce, J. L. McClean, and A. Mahadevan, 2013: Recon-
679 structing the ocean’s interior from surface data. *Journal of Physical Oceanography*, **43** (8),
680 1611–1626.

681 Wortham, C. and C. Wunsch, 2014: A multidimensional spectral description of ocean vari-
682 ability. *J. Phys. Oceanogr.*, **44**, 944–966.

683 Wunsch, C., 2005: The total meridional heat flux and its oceanic and atmospheric partition.
684 *J. Climate*, **18**, 4378–4384.

685 Wunsch, C., 2010: Toward a midlatitude ocean frequency–wavenumber spectral density and
686 trend determination. *J. Phys. Oceanogr.*, **40**, 2264–2282.

687 Xu, Y. and L. Fu, 2012: The effects of altimeter instrument noise on the estimation of the
688 wavenumber spectrum of sea surface height. *J. Phys. Oceanogr.*, **42**, 2229–2233.

List of Figures

- 1 Power spectral density of SST variance as a function of latitude and inverse wavelength (left), frequency (center), and phase speed(right). All color scales are logarithmic. In the left panel, the average tracked-eddy inverse wavelength ($K_{eddy}/2\pi$, from Chelton et al. 2011), the Rossby deformation inverse wavelength ($K_d/2\pi$, from Tulloch et al. 2009), and the Rhines inverse wavelength ($K_\beta/2\pi$) are also plotted. In the right panel, the long Rossby wave phase speed (c_R) and the speed of tracked nonlinear eddies (c_{eddy} , from Chelton et al. 2011) are also plotted. 24
- 2 The same as Fig. 1, but for the SSH-derived meridional velocity. 25
- 3 Cross spectral density $\overline{V\Theta}$ as a function of latitude and wavelength (left), frequency (center), and phase speed(right). Otherwise the same as Fig. 1. 26
- 4 The same as Fig. 1, but for the POP model SSH. 27
- 5 The same as Fig. 2, but for the POP model surface meridional velocity. 28
- 6 The same as Fig. 3, but for the POP model surface meridional temperature flux. 29
- 7 Comparison of $\overline{V\Theta}(c)$ from the satellite data (upper) and POP model (lower) in the extratropics. The long Rossby wave phase speed (c_R) and the speed of tracked nonlinear eddies (c_{eddy} , from Chelton et al. 2011) are also shown. 30

- 708 8 The first moments M_1^k (upper panel) and second moments M_2^k (middle panel)
709 of the wavenumber spectra $\overline{|\Theta|^2}(k)$ (blue), $\overline{|V|^2}(k)$ (green), and $\overline{V\Theta}(k)$ (red).
710 The satellite data are plotted with solid lines, and the POP model is plotted
711 with dashed lines. In the upper panel the wavenumber has been converted to
712 wavelength for plotting. The observed coherent eddy wavelength L_{eddy} (solid
713 black) and the deformation wavelength L_d (dashed black) are also plotted. In
714 the middle panel, the square root of the second moment is shown, indicating
715 the “width” of the spectra in k space. In the bottom panel, the ratio between
716 the observed coherent eddy wavenumber, the deformation wavenumber, and
717 the Rhines wavenumber and $M_1^k(\overline{V\Theta})$ is shown; where this ratio is greater
718 than 1, it means that the heat flux is dominated by scales *larger* than the
719 comparison scale. 31
- 720 9 The same as Fig. 8, but for the c -moments. In the upper panel, the tracked
721 coherent eddy phase speed c_{eddy} (solid black) and the long-wave Rossby wave
722 phase speed from linear theory c_R (dashed black) are also plotted. 32
- 723 10 Meridional heat transport per degree of longitude (upper left), mean merid-
724 ional SST gradient (upper right), eddy kinetic energy (bottom left), and
725 eddy diffusivity (bottom right) from the satellite data (solid) and POP model
726 (dashed). 33

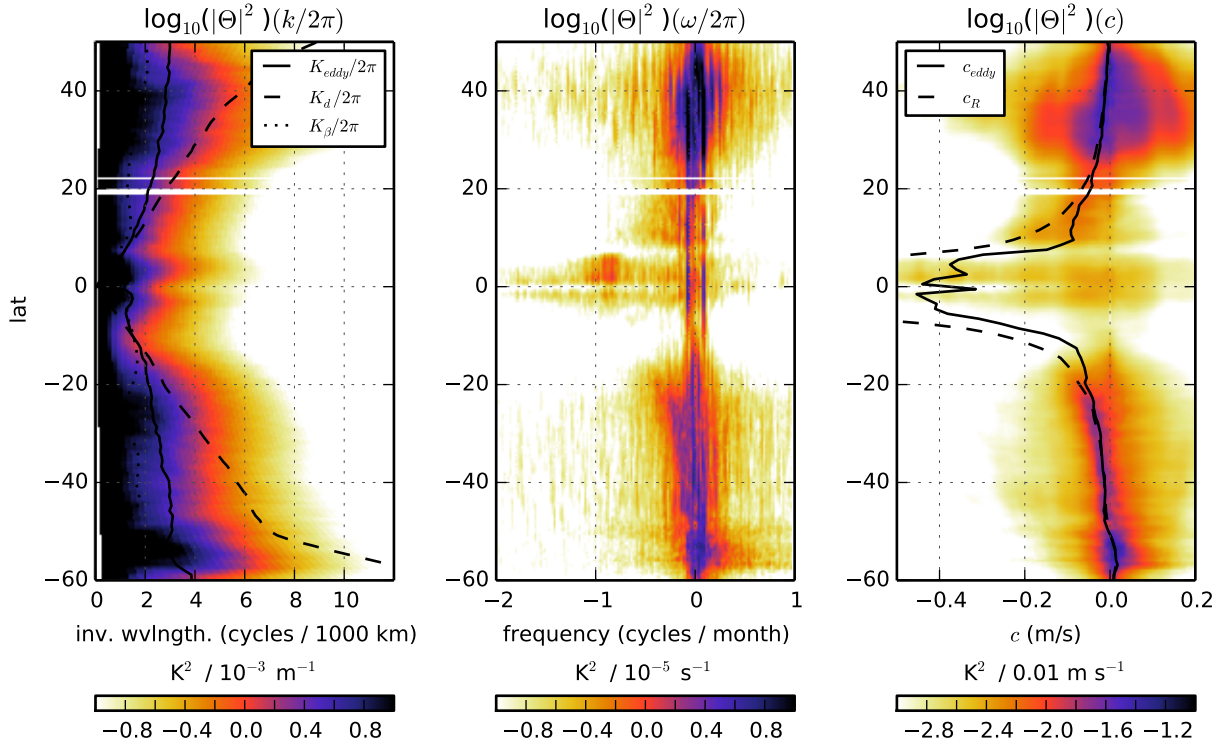


FIG. 1. Power spectral density of SST variance as a function of latitude and inverse wavelength (left), frequency (center), and phase speed(right). All color scales are logarithmic. In the left panel, the average tracked-eddy inverse wavelength ($K_{eddy}/2\pi$, from Chelton et al. 2011), the Rossby deformation inverse wavelength ($K_d/2\pi$, from Tulloch et al. 2009), and the Rhines inverse wavelength ($K_\beta/2\pi$) are also plotted. In the right panel, the long Rossby wave phase speed (c_R) and the speed of tracked nonlinear eddies (c_{eddy} , from Chelton et al. 2011) are also plotted.

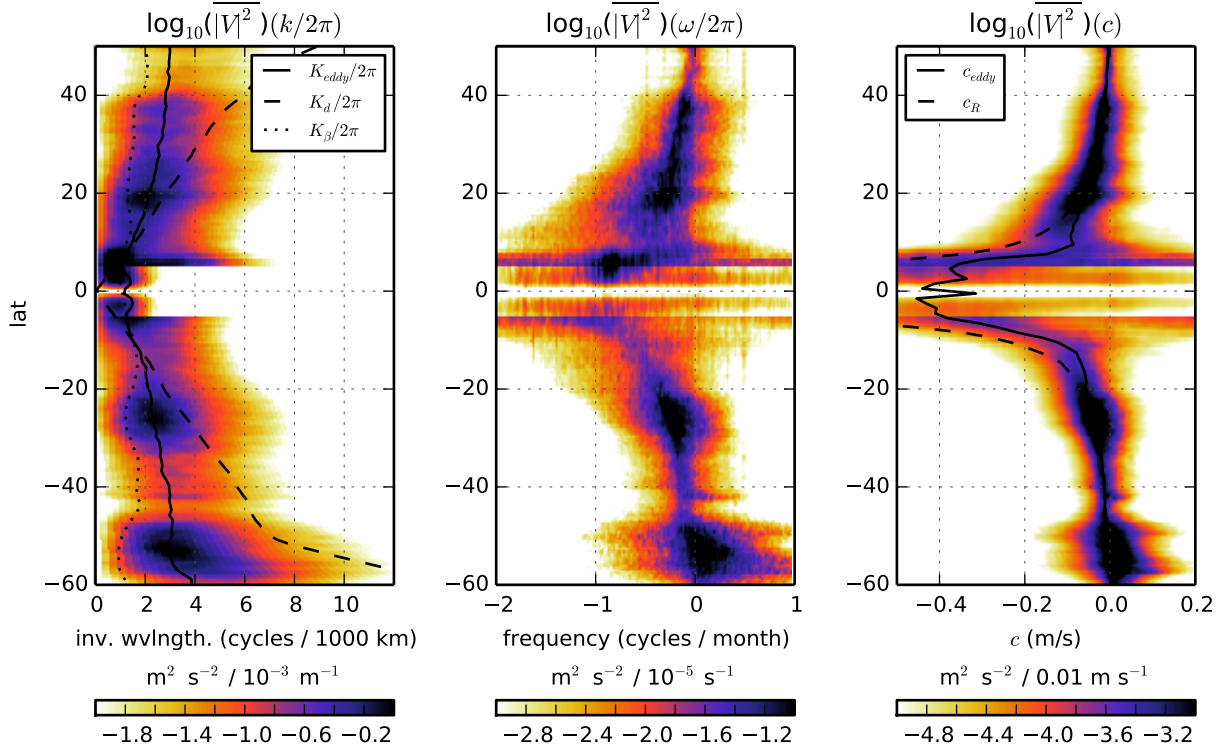


FIG. 2. The same as Fig. 1, but for the SSH-derived meridional velocity.

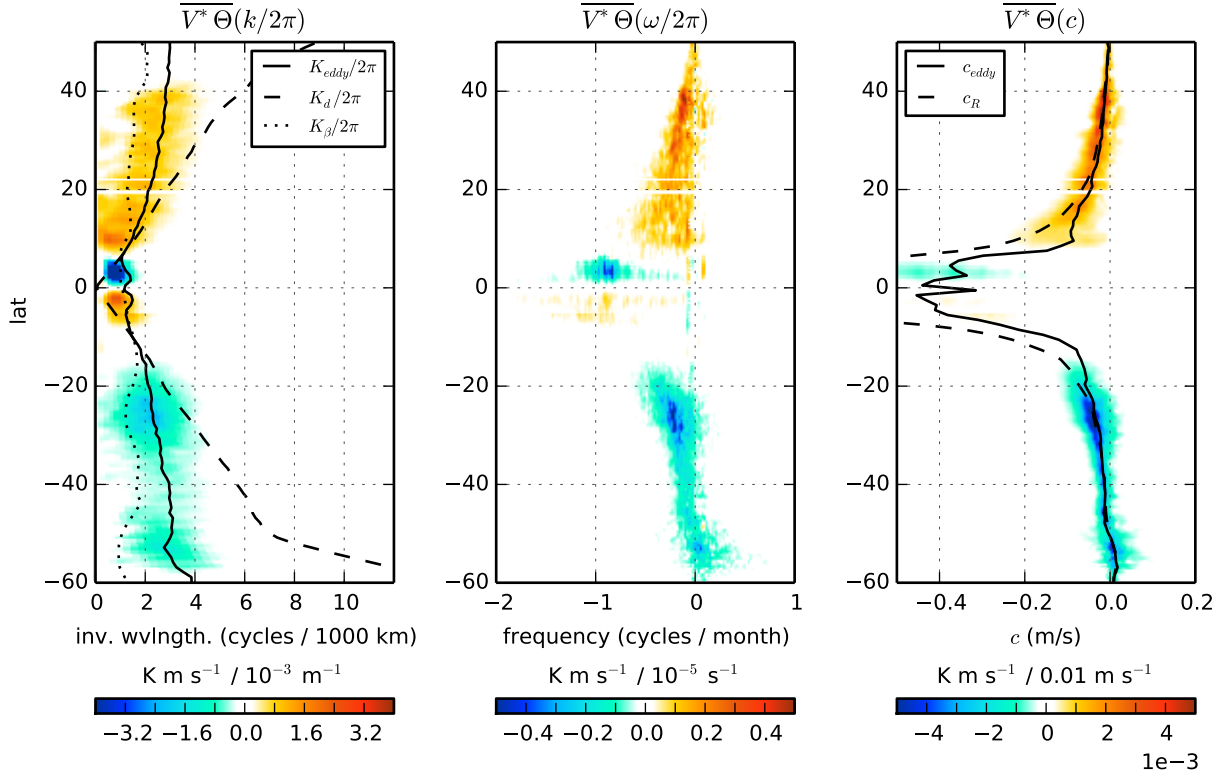


FIG. 3. Cross spectral density $\overline{V^* \Theta}$ as a function of latitude and wavelength (left), frequency (center), and phase speed(right). Otherwise the same as Fig. 1.

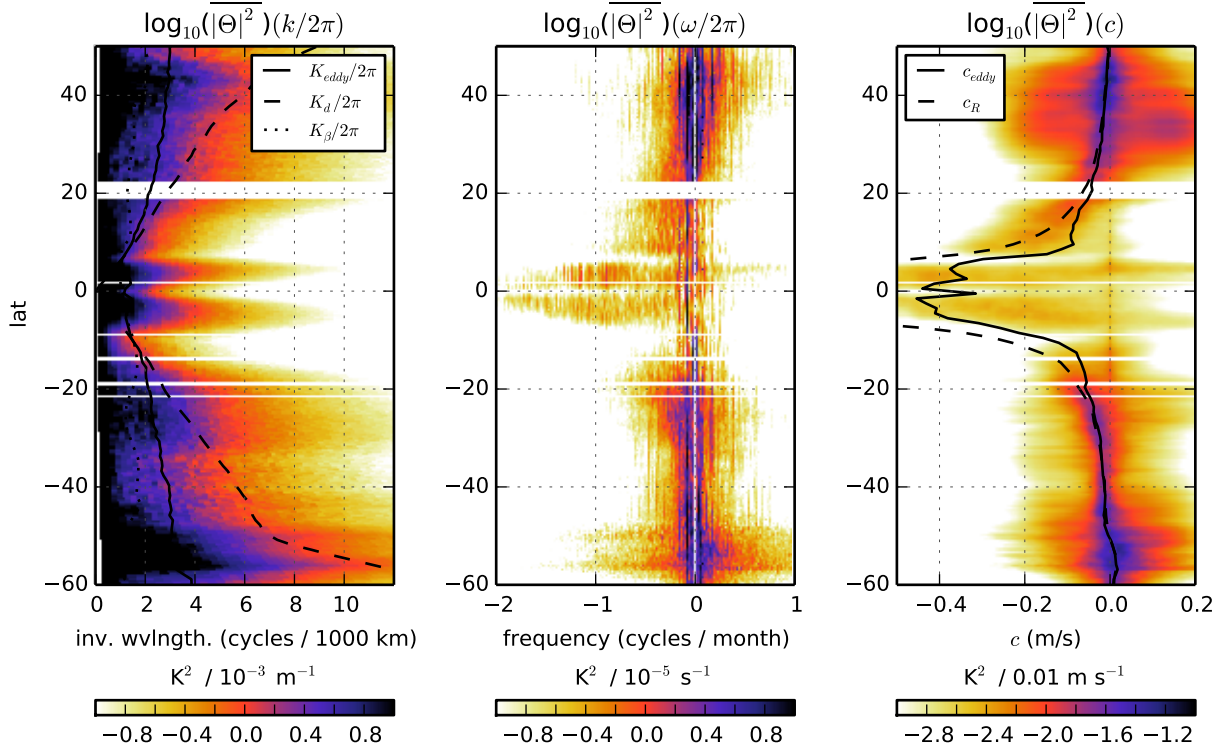


FIG. 4. The same as Fig. 1, but for the POP model SSH.

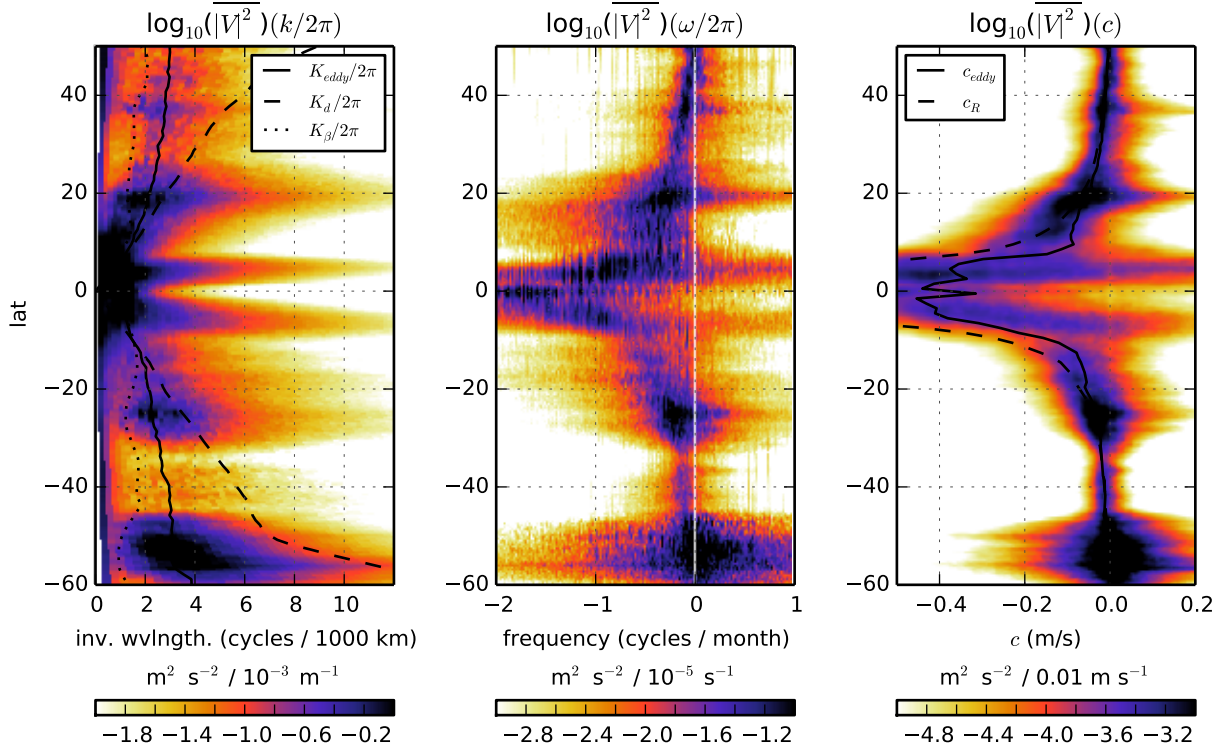


FIG. 5. The same as Fig. 2, but for the POP model surface meridional velocity.

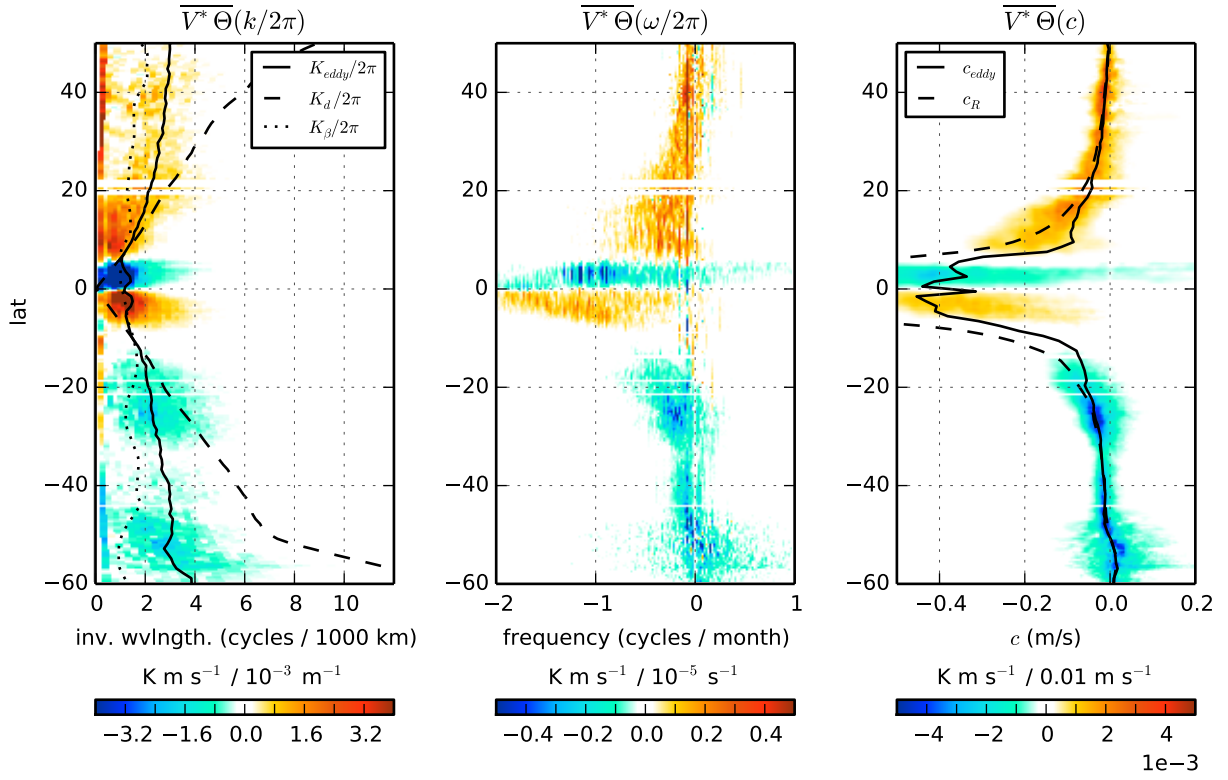


FIG. 6. The same as Fig. 3, but for the POP model surface meridional temperature flux.

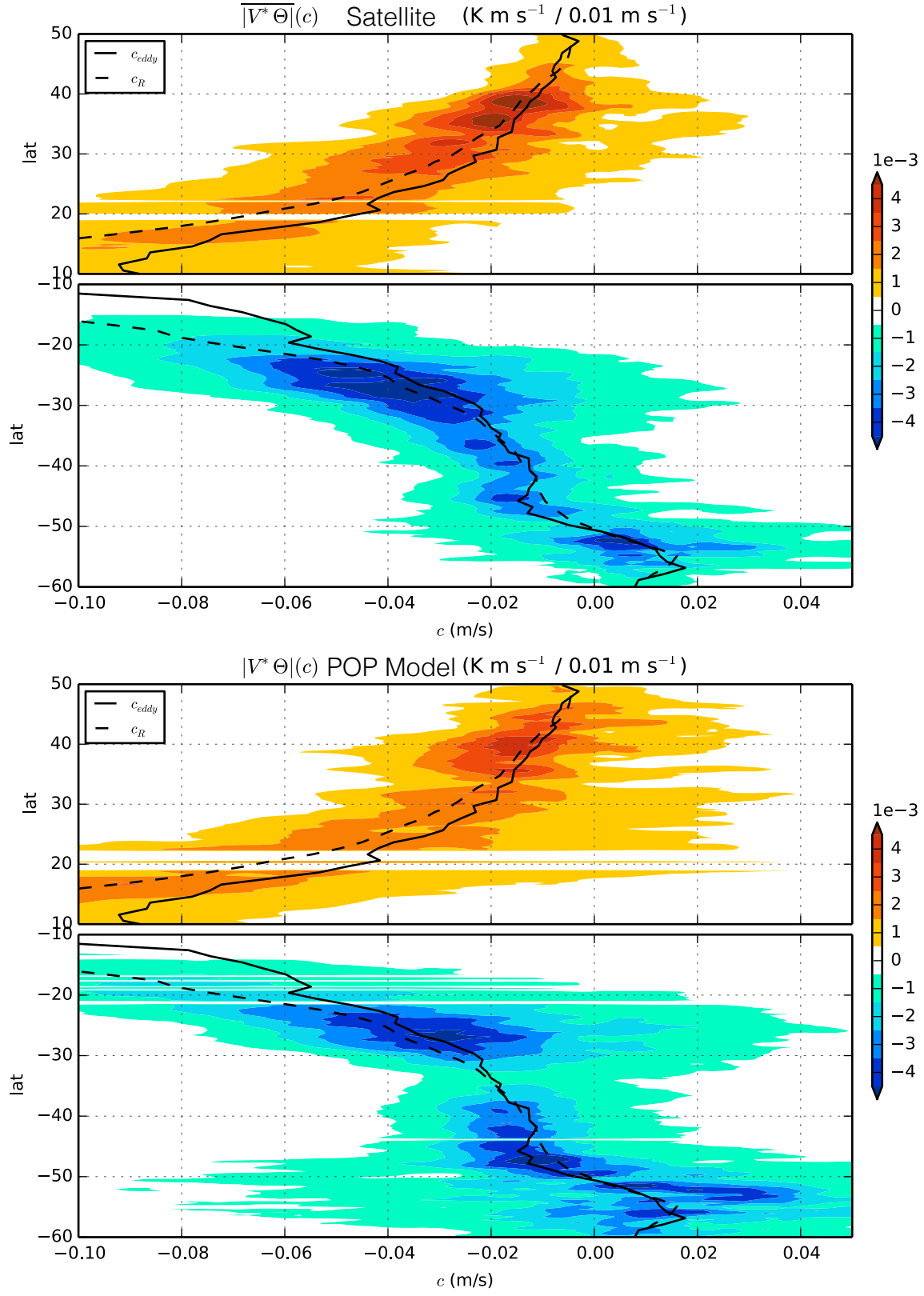


FIG. 7. Comparison of $\overline{V^*\Theta}(c)$ from the satellite data (upper) and POP model (lower) in the extratropics. The long Rossby wave phase speed (c_R) and the speed of tracked nonlinear eddies (c_{eddy} , from Chelton et al. 2011) are also shown.

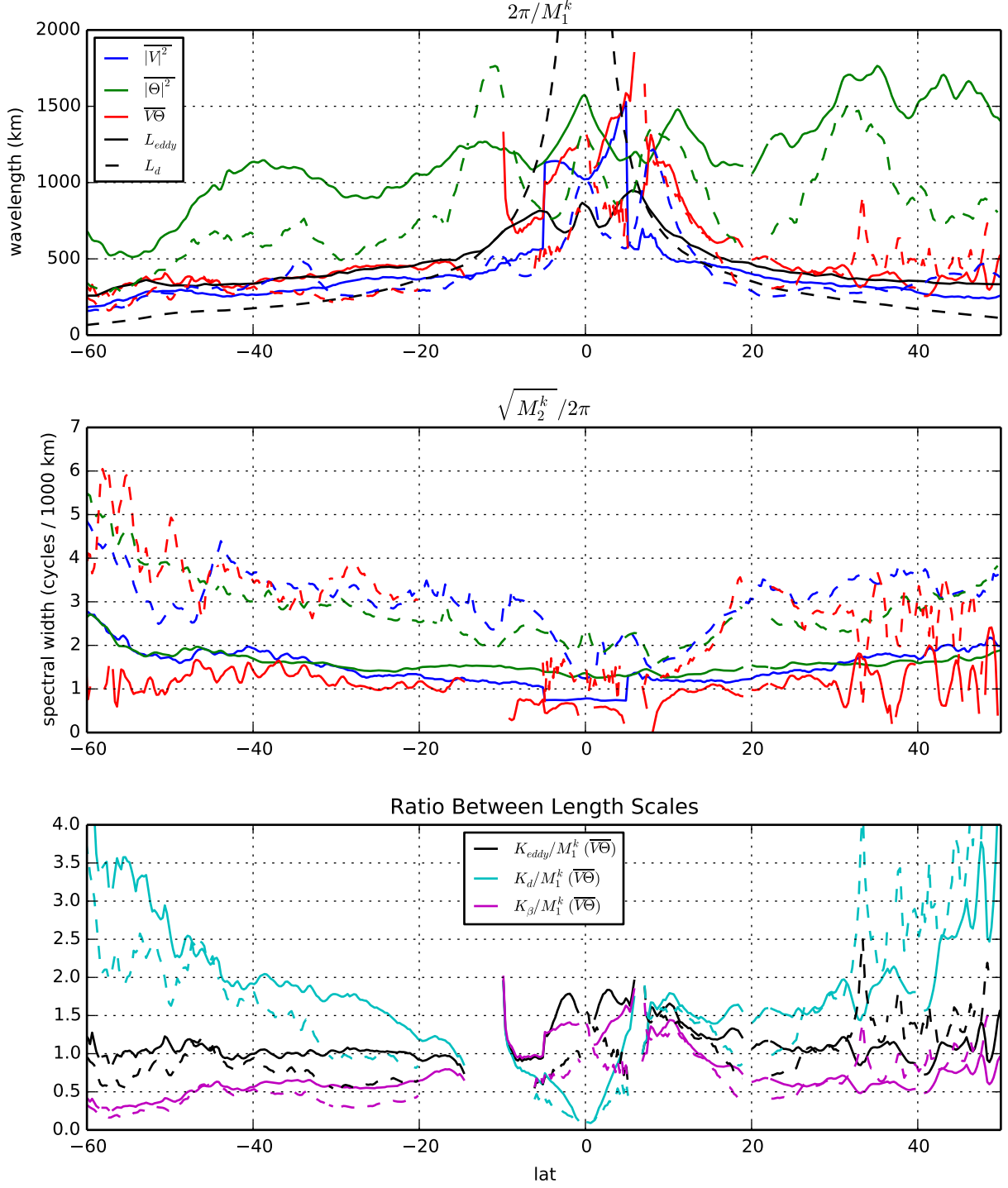


FIG. 8. The first moments M_1^k (upper panel) and second moments M_2^k (middle panel) of the wavenumber spectra $|\bar{\Theta}|^2(k)$ (blue), $|\bar{V}|^2(k)$ (green), and $\bar{V}\bar{\Theta}(k)$ (red). The satellite data are plotted with solid lines, and the POP model is plotted with dashed lines. In the upper panel the wavenumber has been converted to wavelength for plotting. The observed coherent eddy wavelength L_{eddy} (solid black) and the deformation wavelength L_d (dashed black) are also plotted. In the middle panel, the square root of the second moment is shown, indicating the “width” of the spectra in k space. In the bottom panel, the ratio between the observed coherent eddy wavenumber, the deformation wavenumber, and the Rhines wavenumber and $M_1^k(\bar{V}\bar{\Theta})$ is shown; where this ratio is greater than 1, it means that the heat flux is dominated by scales *larger* than the comparison scale.

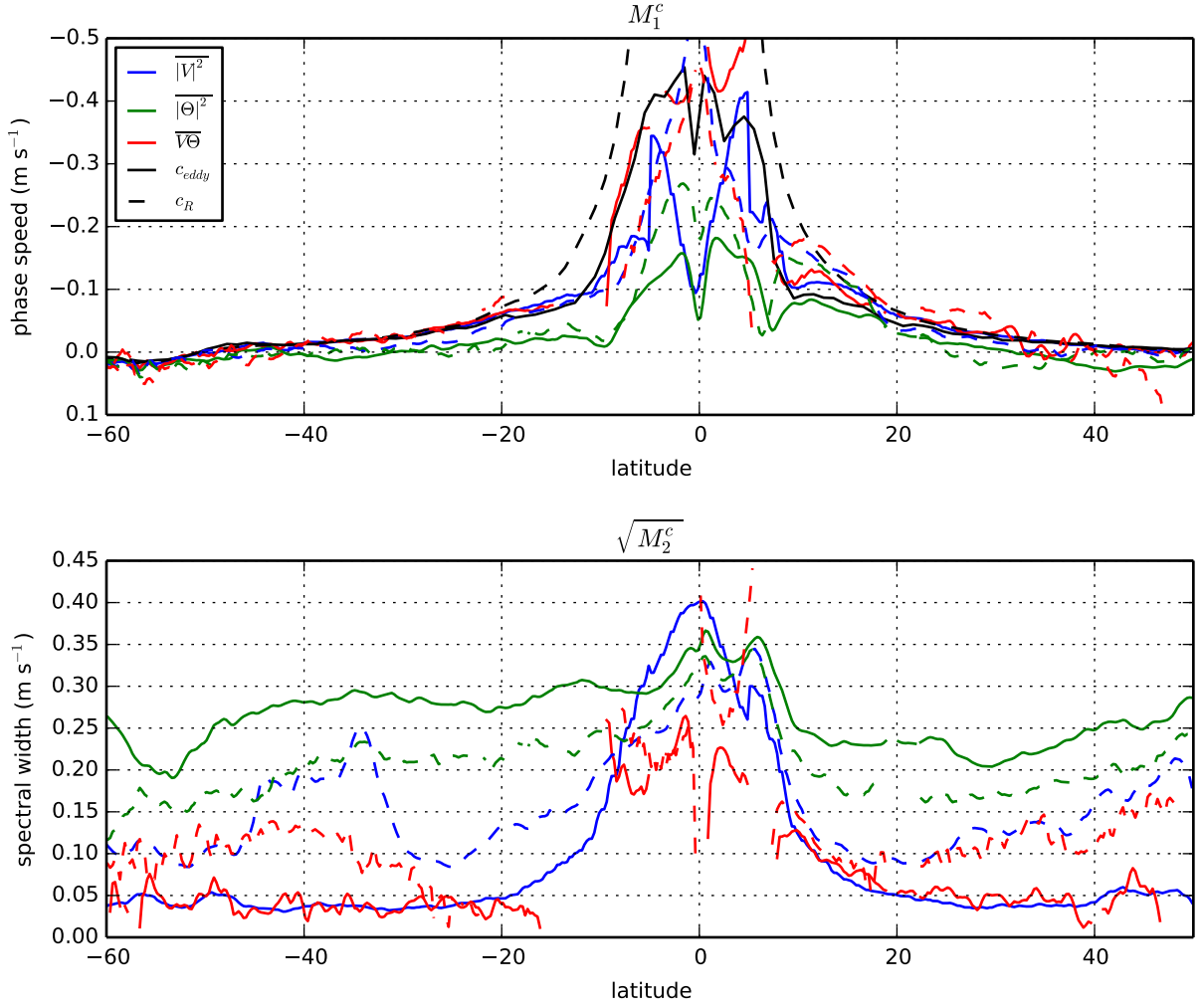


FIG. 9. The same as Fig. 8, but for the c -moments. In the upper panel, the tracked coherent eddy phase speed c_{eddy} (solid black) and the long-wave Rossby wave phase speed from linear theory c_R (dashed black) are also plotted.

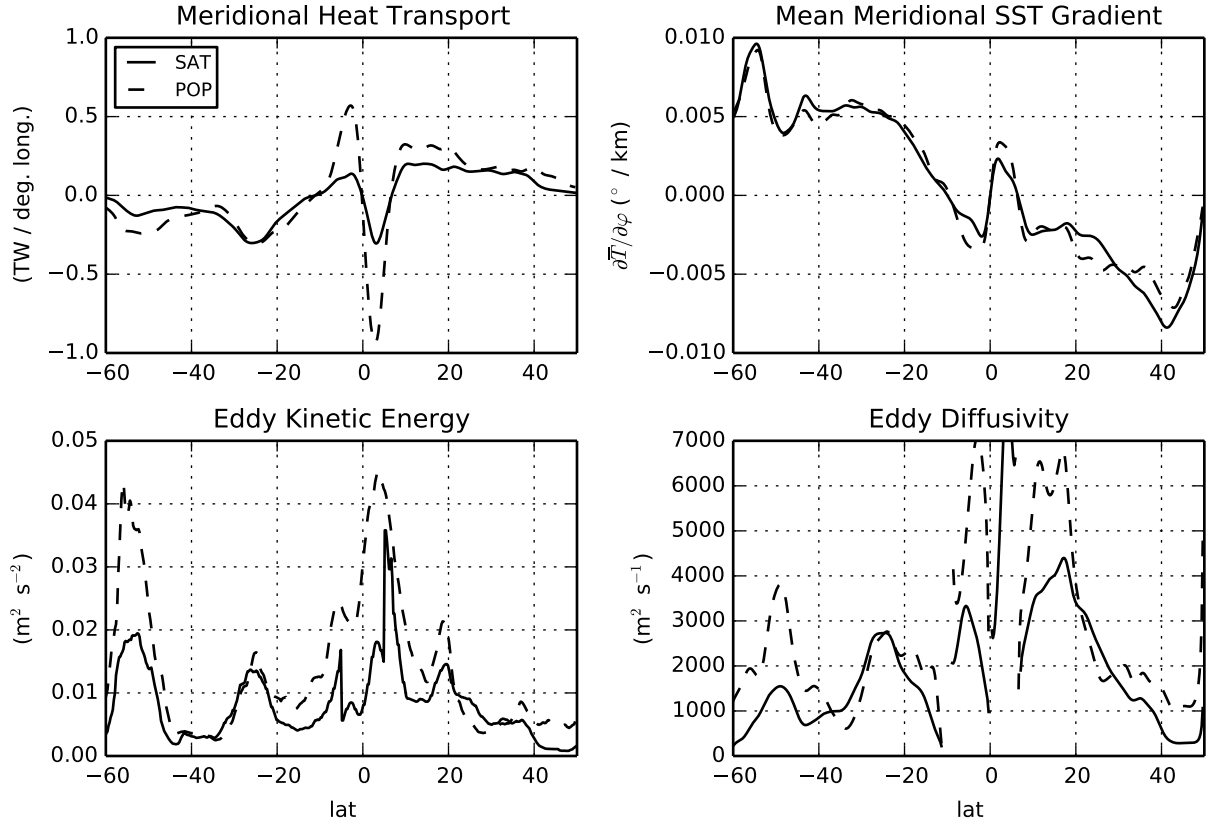


FIG. 10. Meridional heat transport per degree of longitude (upper left), mean meridional SST gradient (upper right), eddy kinetic energy (bottom left), and eddy diffusivity (bottom right) from the satellite data (solid) and POP model (dashed).